

Parallel Convection and ExB Drifts in the TCV Snowflake Divertor and their effects on target heat-fluxes.

C. K. Tsui¹, J. A. Boedo¹, D. Galassi², J. Loizu², R. Maurizio², H. Reimerdes², B.P. Duval², O. Février², M. Spolaore³, M. Wensing², the TCV Team⁴, and the Eurofusion MST1 Team⁵

¹Center for Energy Research (CER), University of California-San Diego (UCSD), La Jolla, California 92093, USA

²Ecole Polytechnique Fédérale de Lausanne (EPFL), Swiss Plasma Center (SPC), CH-1015 Lausanne, Switzerland

³Consorzio RFX, Euratom-ENEA Association, Corso Stati Uniti 4, IT-45127 Padova, Italy

⁴See author list of S. Coda et al 2019 Nucl. Fusion 59 112023

⁵See the author list of B. Labit et al 2019 Nucl. Fusion 59 086020

Parallel convection and ExB drifts act together to redistribute heat between the strike-points in the Low Field Side Snowflake Minus (LFS SF-). The cumulative heat convection from both mechanisms is enhanced near the secondary X-point and is shown to dominate over heat conduction, partly explaining why the LFS SF- distributes power more evenly than the single null or other snowflake configurations. Pressure profiles at the entrance of the divertor are strongly affected by the position of the secondary X-point and magnetic field direction indicating the importance of ExB drifts. Pressure drops of up to 50% appear between the outer-midplane (OMP) and the divertor entrance enhancing the role of parallel heat convection. The electron temperature and density profiles and the radial turbulent fluxes measured at the OMP are largely unaffected by the changes in divertor geometry, even on flux surfaces where the connection length is infinite.

(Some figures may appear in color only in the online journal)

1 Introduction

Mitigating the large heat and particle fluxes in tokamak divertors presents a major outstanding problem for future fusion reactors such as ITER and DEMO for which unmitigated heat-fluxes are projected to exceed the target engineering limits which could be as low as 5 MW/m²[1–3]. The snowflake (SF) divertor configuration has been proposed as a possible solution to reduce peak heat fluxes on the plasma-facing components[4], and has been the subject of extensive study[5–11]. The exact snowflake features a second-order null-point where the poloidal cross-section of the separatrix forms a hexagonal structure evocative of a snowflake, as shown in Figure 1a. In practice, the second-order null-point splits into two nearby first-order null-points (X-points) where the primary X-point lies on the Last Closed Flux Surface (LCFS). If the secondary X-point is located in the private flux region, the configuration is sub-classified as a ‘snowflake plus’ (SF+) [12] as shown in Figure 1b. Compared to the Single Null (SN), the exact SF and the SF+ have the advantages of power distribution to two additional (secondary) strike-points, control over the poloidal flux-expansion at the target, increased connection lengths $L_{||}$, and a smaller magnitude of the poloidal field B_{θ} over a wider divertor volume that is predicted to enhance cross-field transport [13]. These modifications are predicted to provide access to stronger detachment for the same upstream conditions [14,15], as confirmed by experiments [7,9,10,16–19], though further work is necessary in order to disentangle the effects of the snowflake divertor from those of flux flaring [20]. However in L-mode conditions, the secondary strike-points of the exact snowflake only receive up to 10% of the divertor power [17,21,22].

If the secondary X-point is in the common flux region of the SOL the divertor geometry is sub-classified as a Snowflake Minus (SF-) such as the Low-Field Side Snowflake Minus (LFS SF-) shown in Figure 1c. In this magnetic geometry, three of the strike-points are directly connected to the common flux region and the outer SOL is bifurcated by the secondary X-point and its corresponding secondary separatrix. By splitting the SOL, the SF- can be highly effective at decreasing the peak heat fluxes, albeit only on one side of the divertor. This geometrical power splitting can be described using only the heat-flux fall off length λ_q and the distance between the primary and secondary separatrices (dR_{x2}) measured at the Outer Midplane (OMP) using a ‘simple geometrical-diffusive’ model [23]; which has been shown to agree with simulations without drifts [15,24], Spitzer Heat Conduction estimates [25], and measurements in the High Field Side (HFS) SF- [26].

However, infrared (IR) camera measurements show that the LFS SF- divides power between SP2 and SP4 more evenly than predicted by the geometrical model [26]. The outer target was shown to have a $\lambda_q^{eff}=9\text{mm}$, which was $>2\times$ wider than reference SN divertors, demonstrating a broadened heat-flux footprint and suggesting that enhanced cross-field transport is moving heat towards SP4. E.g. for $dR_{x2}=6\text{mm}$, the model predicts a power splitting fraction $f_{split} = P_{sp4}/(P_{sp2} + P_{sp4})$ of 23%, but measurements give $f_{split} = 50\%$. Figure 10a in Ref [26] at $dR_{x2}=6\text{mm}$ shows that P_{sp4} exceeds the Spitzer conduction prediction by more than a factor of 2.

This paper aims therefore to explore the mechanisms responsible for the improved power splitting in the LFS SF- using the first (to our knowledge) reciprocating probe measurements near the snowflake nulls. Section 3 demonstrates that the changes in heat-flux distribution are not due to changes in the upstream T_e or n_e profiles. In section 4, the pressure profiles at the entrance to the outer divertor are shown to depend on divertor geometry and field direction suggesting that ExB drifts are important. The pressure is shown to drop by up to 50% compared to the OMP suggesting that strong parallel flows are being driven. In section 5, these effects are explored in detail and it is shown that the secondary separatrix enhances the ExB drift and reverses the parallel flow such that these convective mechanisms act together to drive particles and heat towards the secondary X-point and SP4. Quantifying these effects shows that convection likely explains the improved power-splitting of the LFS SF-.

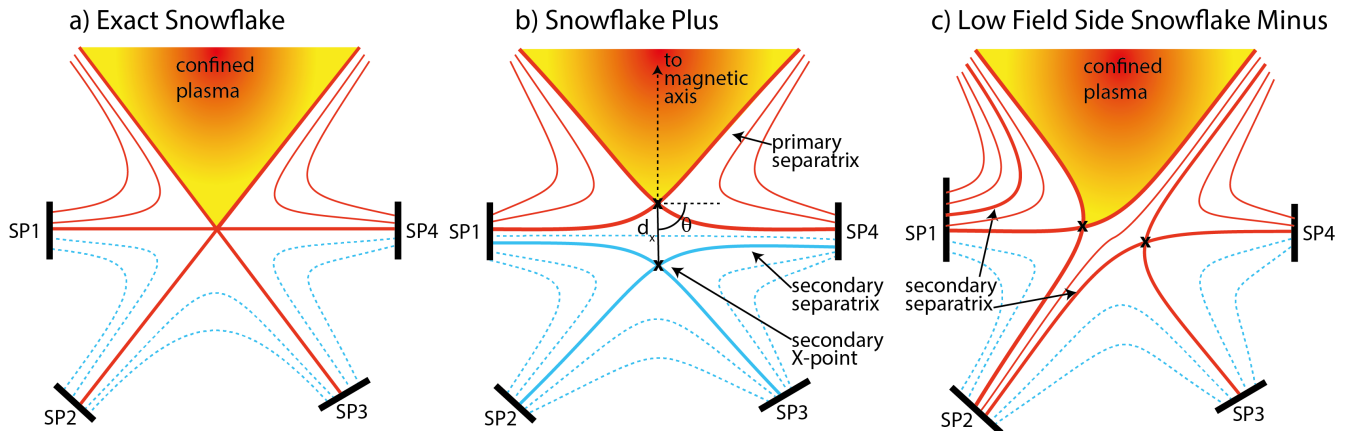


Figure 1 Illustrations of the geometries for the (a) exact snowflake, (b) the snowflake plus, and (c) the low field side snowflake minus. The thick lines represent separatrixes, red lines represent magnetic flux surfaces in the Common Flux Region (CFR) of the Scrape-off Layer (SOL), and blue lines represent flux surfaces without parallel connections to CFR i.e. in the Private Flux Regions (PFR).

2 Experimental Setup

The experiments were performed in the Tokamak à Configuration Variable (TCV)[27], which has a highly-elongated vacuum vessel and 16 independently powered poloidal field coils allowing access to a wide range of alternative divertor configurations, as well as a large variation in the vertical position of the plasma. Two example LFS SF- geometries with the magnetic axis height Z_{mag} translated by 36cm are shown in Figure 2. This allowed the reciprocating probe [28] mounted horizontally at $Z=0$ to take measurements at the OMP and just above the X-points at the divertor entrance. The relative position of the primary and secondary X-points were modified to keep SP4 out of diagnostic ports while still allowing the reciprocating probe to reach the Last Closed Flux Surface (LCFS).

The discharges were operated in forward-field forward- I_p (toroidal field $B_t = -1.4\text{T}$, $B \times \nabla B$ downward, plasma current $I_p = -235 \pm 10$ kA) or reverse-field reverse- I_p ($B_t = 1.4\text{T}$, $B \times \nabla B$ upward, $I_p = 235 \pm 10$ kA). The line-integrated densities were held constant at $\langle n_e \rangle = 3.9\text{e}19 \pm 0.3\text{e}19 \text{ m}^{-3}$ in order to access the conduction-limited regime with typical median values of the SOL collisionality parameter $\nu_{\text{SOL}}^* \sim 25$ across the width of the SOL (not including regions $< 2\text{mm}$ from a separatrix) where $\nu_{\text{SOL}}^* \approx 10^{-16} n_e [\text{m}^{-3}] L_{\parallel} [\text{m}] / T_e^2 [\text{eV}]$, the electron density n_e , temperature T_e , and connection length L_{\parallel} are taken at the OMP. The conduction-limited regime (when the parallel heat flux is expected to be dominated by its conductive component) is defined for $10 < \nu_{\text{SOL}}^* < 85$ [29]. These conditions are identical to those described in Ref [26] where detailed descriptions of the infrared camera data and radiative losses are available.

The reciprocating probe head consists of ten electrodes (see geometry in Figure 3) which were used in groups to provide a variety of diagnostic functions. The double probe was used to determine T_e and n_e while accounting for sheath expansion [30] with a sweep frequency of 1 kHz. The Mach probes were used to determine the Mach number M_{\parallel} as described in Ref [31]. The I_{sat} and V_f electrode array were sampled at 2.5-5 MHz to measure the properties of the plasma turbulence and the radial turbulent flux Γ_r^{turb} following the procedures outlined in refs [32–34]. The probe head was rotated along the \hat{R} axis to maintain alignment with the magnetic field within $\pm 5^\circ$.

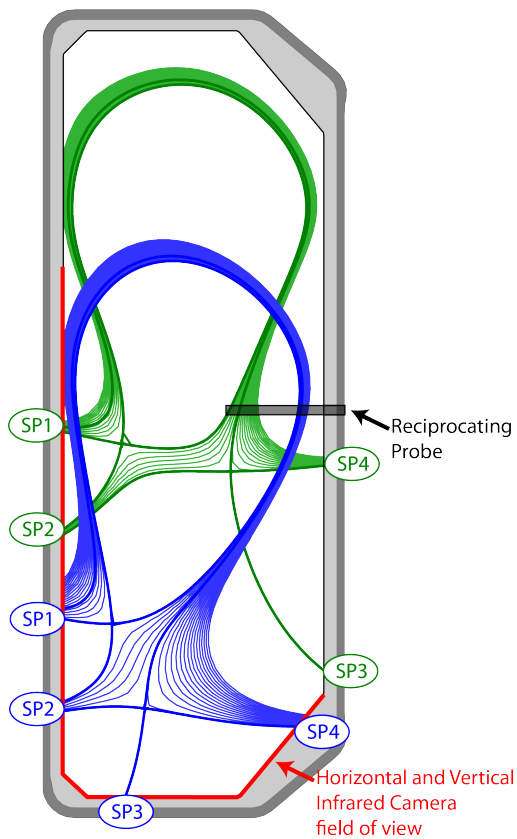


Figure 2 The poloidal cross-section of the TCV vessel with two example equilibrium reconstructions of LFS SF- discharges at different vertical positions. The measurement location of the reciprocating probe is shown in black, and the IR camera coverage from the overlapping field of view from three vessel ports is shown in red.

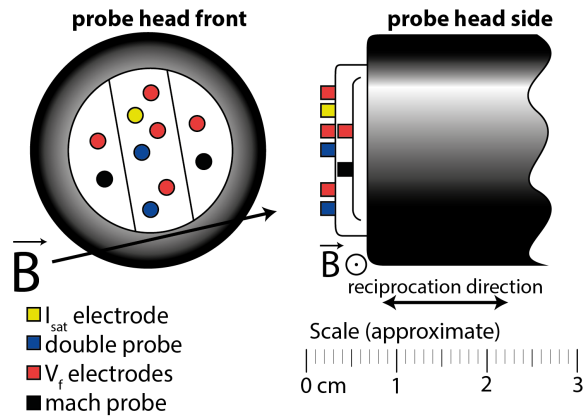


Figure 3 A diagram of the head of the reciprocating probe illustrating the geometry and orientation of the electrodes used for the various measurements.

3 Upstream Profiles are Unaffected by Divertor Geometry

To begin, the plasma conditions at the OMP are compared for a variety of divertor configurations. Target heat fluxes depend strongly on upstream conditions (e.g. $q_{||} \propto T_e^{7/2}$) so even small changes at the OMP are important. Figure 4 shows a comparison between the SF+, HFS SF-, LFS SF-, and a reference SN divertor plotted as functions of the distance from the primary separatrix normalized to the OMP ($R-R_{sep}$). The connection lengths (a,b) show little difference between the SF+ and the SN. In contrast, the LFS SF- and HFS SF- provide a 2x increase in $L_{||}$ for the first several millimeters on their respective sides with a singularity at the location of the secondary separatrix dR_{x2} . The I_{sat} profiles (c) for the four divertor geometries match within the statistical scatter due to plasma fluctuations as represented by the shaded region the $\pm 1\sigma$ boundaries. No significant differences are observed in the n_e (d), and T_e (e) profiles for any of the 4 geometries. Finally, the radial turbulent particle fluxes Γ_r^{turb} shown in subplot (f) indicate that any differences are marginal compared to the scatter in the measurements.

The similarity between the upstream profiles is an unexpected result considering that $L_{||}$ has been modified by a factor of ~ 2 , the major radius of the target R_t by a factor of 1.8, and the flux-expansion at the target has variations over a factor of 3. Additionally, the divertor configurations have differences in divertor volumes, magnetic shear, and target field-line angles. Significant changes were made both on the HFS and the LFS. None of these modifications, nor their combinations have a significant effect on the profiles at the OMP. This suggests that any changes brought about in the plasma conditions within the divertor are effectively smoothed out by the cross-field transport near the OMP. Additionally, changes made in geometry on one side of divertor may be counteracted by the plasma conditions in the other side of the divertor, as has been observed when comparing the inner and outer divertor conditions in the SN[35]. These results show that when simulating alternative divertor configurations in TCV, it is appropriate to use the same upstream conditions for all divertor configurations. The improved power splitting in the LFS SF- is not caused by changes in upstream plasma conditions.

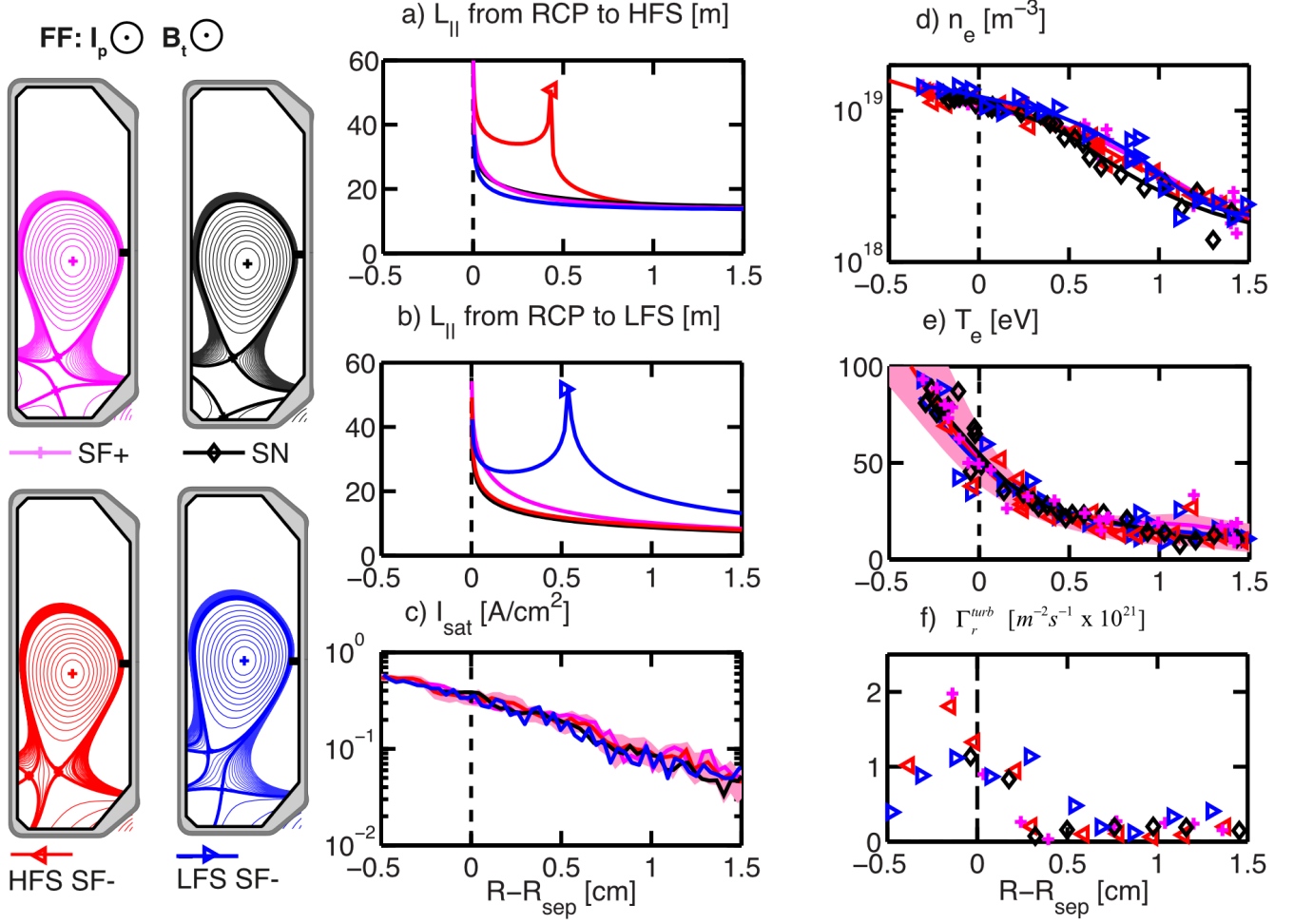


Figure 4 Magnetic equilibrium reconstructions (left) and profiles (right) are compared between a SF+ discharge (magenta +), a HFS SF- discharge (red <), a LFS SF- discharge (blue >), and a similar Single Null reference (black \diamond) in Forward Ip & Bt measured at the OMP. The connection lengths to the LFS (a) and HFS (b) are calculated from the probe location using the magnetic reconstruction. A 0.4mm bin-average is shown for I_{sat} (c), while spline fits are shown for n_e (d) and T_e (e). The radial turbulent flux Γ_r^{turb} is shown in (f). Markers are included where convenient to identify the lines. The shaded regions represent 1σ in the I_{sat} scatter (due to turbulent fluctuations) (c) and the 1σ uncertainty from the fit algorithm in (e). Individual data points are plotted in (d-f) to show the uncertainties and the tension of the spline fits. The x-axis flux coordinate ($R - R_{sep}$) is the distance from the primary separatrix measured at the OMP.

4 Pressure Gradients indicate the importance of Drifts and Parallel Convection

While the temperature and density profiles at the OMP are unaffected by divertor geometry, they vary significantly downstream at the entrance of the divertor. Reciprocating probe profiles were taken at the divertor entrance of the LFS SF- in forward field (Figure 5 top row), and reverse field (Figure 5 bottom row). These profiles are 0.35m below the magnetic axis (marked by the + at the center of the plasma) which corresponds to a parallel distance of 3.4m, which is up to 20% of the total $L_{||}$. Compared to the smooth profiles at the OMP (black lines) the I_{sat} profiles near the divertors (red & green lines) pivot sharply at the secondary separatrices (dashed lines at dR_{x2}). In forward field a drop in I_{sat} is observed between the OMP and the divertor entrance outside of the secondary separatrix denoted by the green

dashed line (Figure 5a). The I_{sat} measurements can be considered as a proxy for the electron pressure as $I_{\text{sat}} \propto p_e / \sqrt{T_e}$ and has smaller uncertainties than the processed plasma parameters such as n_e and T_e . Therefore, a statistically significant drop in p_e of up to 50% is observed outside of the secondary separatrix in forward field which is caused by a drop in n_e (c) while T_e (e) has not changed significantly compared to the OMP.

In reverse field, however, a different pattern is observed where there is a drop in electron pressure and a flat n_e profile for $R-R_{\text{sep}} < dR_{x2}$, which is especially strong at the primary separatrix (see Figure 5b,d). These measurements are reproducible across repeat discharges (red dashed lines). Measurements also show a drop in T_e (f) of up to 10eV for $0.2\text{cm} < R-R_{\text{sep}} < 1.0\text{cm}$. While any changes to the I_{sat} and T_e profiles at the OMP are largely unaffected by divertor geometry, the profiles at the divertor entrance depend on both the divertor geometry and the field direction.

In the near-SOL close to the LCFS the sign of the n_e imbalance changes with field direction and is consistent with the direction of the poloidal $E_r \times B$ drift (i.e. towards (away from) the outer divertor in forward (reverse) field in the common flux region) and the $B \times \nabla B$ drift (downward in forward field, upward in reverse field). This suggests that drifts are driving the pressure gradients in the near-SOL. Returning parallel flows (i.e. opposing the $E_r \times B$ drift) are measured in this region and it will be shown in section 5 that the parallel fluxes do not fully return the $E_r \times B$ fluxes. However, further study is needed to determine if the pressure gradients are driven directly by the drift-based fluxes, or indirectly via changes in recycling, ionization, or radial transport. It is also noted that ion pressure measurements would be needed to fully understand these pressure gradients. In the far-SOL ($R-R_{\text{sep}} > dR_{x2}$) the parallel fluxes flow towards the target and down the pressure gradient independently of field direction suggesting that both gradient and flow are driven by the plasma sink at the target.

The presence of electron density and pressure gradients above the divertor indicate that both drifts and parallel flows are playing important roles in convecting particles around the SOL. In section 5 we will quantify the effects of the $E_r \times B$ drift and the parallel flows and consider their effects to the heat-flux distribution at the divertor targets.

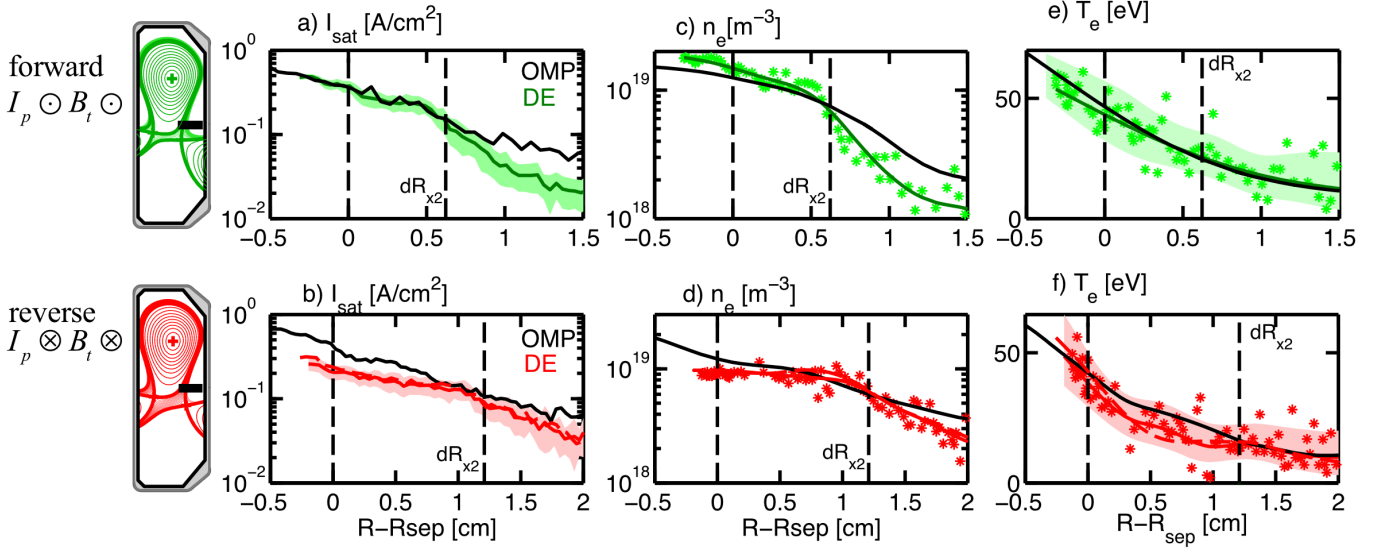


Figure 5 Profile comparisons of I_{sat} (a,b), n_e (c,d), and T_e (e,f) for LFS SF- discharges between the OMP and the divertor entrance. The lines in (a,b) represent 1mm bin-averages, where the shaded region represents the 1σ scatter in the I_{sat} fluctuations. For n_e and T_e the lines represent spline fits, and the shaded region represents the 1σ uncertainty from the I-V fits. The dashed and solid red lines represent separate RCP measurements taken in identical discharges. The location of the secondary separatrix dR_{x2} is marked by a vertical dashed line.

5 Redistribution of Power and Particles via ExB drifts and Parallel Convection in the LFS SF-

In this section, the convected heat-fluxes are quantified in order to consider whether convection is responsible for the improved heat distribution of the LFS SF-. It will be shown that the poloidal $E_r \times B$ drift is enhanced and the parallel flow reverses near the secondary separatrix. This causes the two convective terms to act together driving power and particles towards SP4.

Comparisons are made between measurements taken at the divertor entrance of a single null reference (Figure 7 left column) and a LFS SF- (right column) in forward field. The thin lines map out the first 15mm of the SOL (i.e. 15 flux surfaces spaced 1mm at the OMP), and the region where measurements were taken is represented by the black rectangle. The LFS SF- shown in (b) has a secondary separatrix splitting the outer divertor at $dR_{x2} = 0.6\text{cm}$. IR camera measurements show that this dR_{x2} splits the power evenly between SP2 and SP4 with $f_{\text{split}} = P_{\text{sp4}} / (P_{\text{sp2}} + P_{\text{sp4}}) = 50\%$ [26], which is indicated in Table 1. The estimated conducted power P_{cond} (described below in eqn 5) has a reasonable match with P_{IR} for SP2 ($P_{\text{cond SP2}} = 24\text{kW}$, $P_{\text{IR SP2}} = 29\text{kW}$), but only accounts for a small fraction of the power at SP4 ($P_{\text{cond SP4}} = 9\text{kW}$, $P_{\text{IR SP4}} = 29\text{kW}$). Note that the SN reference has a second X-point, but with $dR_{x2} = 2.9\text{cm}$ it is well outside the region of interest.

	SP1	SP2	SP3	SP4
P_{IR} [kW] [26]	27	29	0	29
P_{cond} [kW]	39	24	0	9
P_{ExB} [kW]	n/a	19	n/a	10
$P_{M_{ }}$ [kW]	n/a	-15	n/a	1
$P_{\theta}^{conv net}$ [kW]	n/a	4	n/a	11

Table 1 The integrated heat fluxes measured or predicted for each strike-point of the LFS SF- with $dR_{x2}=6\text{mm}$ in forward I_p & B_t . P_{IR} from the IR camera has been included for each strike-point. P_{cond} was calculated for each strike-point from T_e measurements at the OMP. P_{ExB} and $P_{M_{||}}$ were calculated at the divertor entrance for SP2 and SP4.

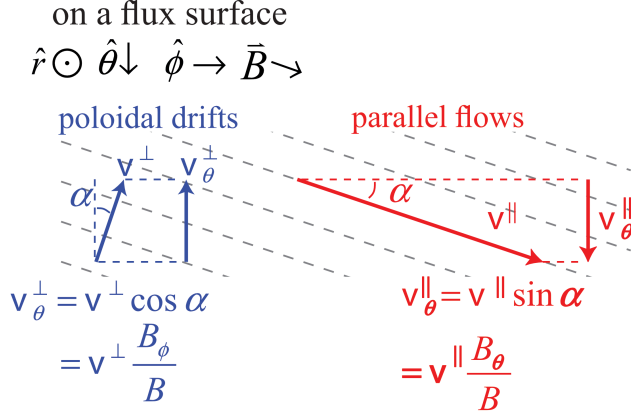


Figure 6 The geometry for poloidal projections. The grey dashed lines represent the magnetic field lines of a flux surface, while the arrows represent the poloidal drifts (left blue), the parallel flows (right red) and their poloidal projections v_{θ}^{\perp} , v_{θ}^{\parallel} .

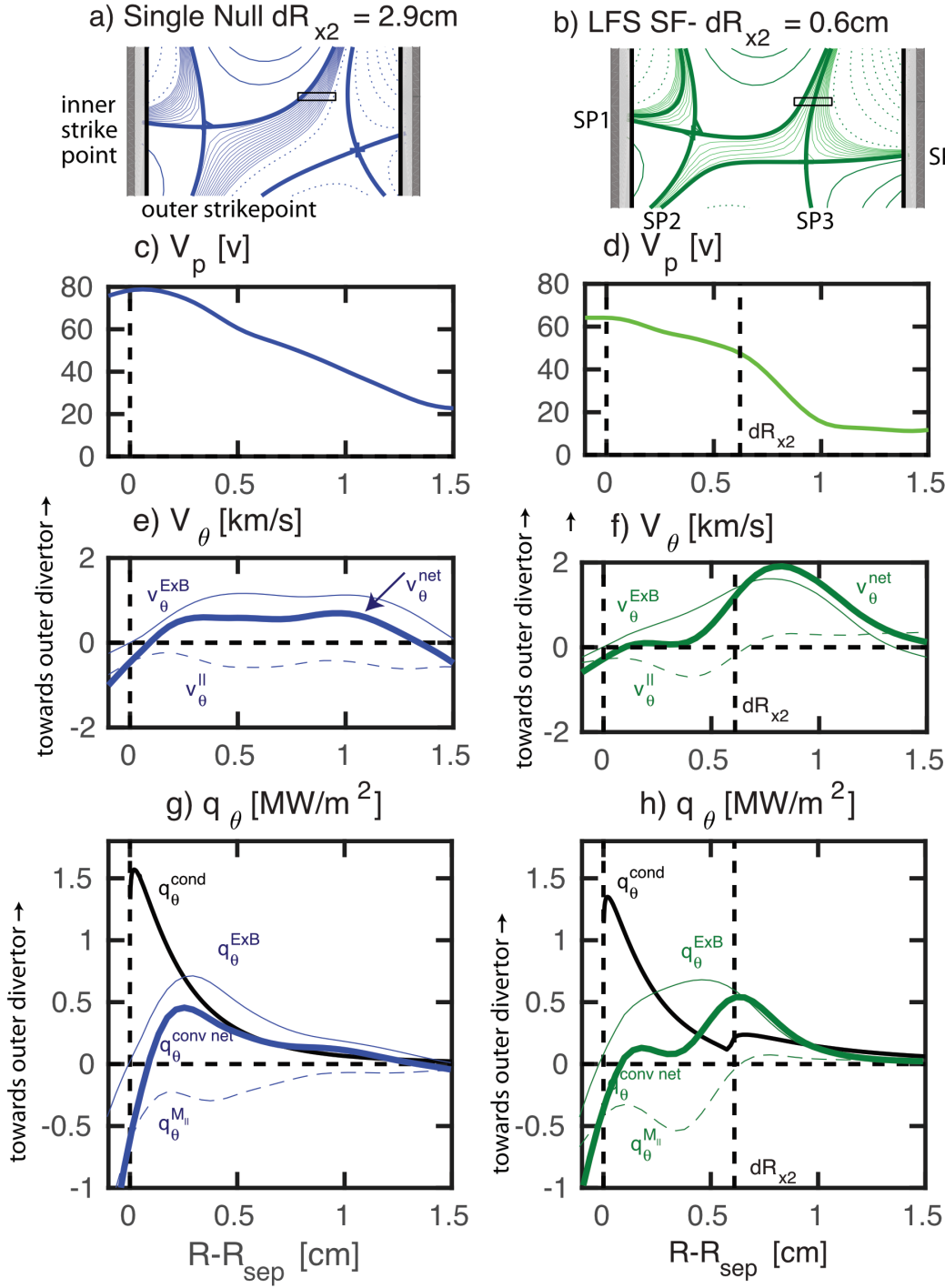


Figure 7 Plasma convection measured at the divertor entrance of a reference single null (left column) and a LFS SF- (right column). The divertor geometries (a,b) show the separatrices and X-points (thick lines). The first 15 mm of the SOL are mapped by thin lines and the measurement location is represented by the black rectangles. The plasma potential profiles (c,d) are used to calculate the E_r . The poloidal projections of the ExB drift velocity v_θ^{ExB} and the parallel flows $v_\theta^{||}$ are shown in (e,f). The poloidal projection of the convected heat fluxes q_θ^{ExB} , $q_\theta^{M||}$, and their sum $q_\theta^{conv net}$ are plotted in (e,f) against the Spitzer conduction heat-flux q_θ^{cond} estimated using upstream reciprocating probe measurements.

Measurements indicate that there are two main components of plasma convection in the SOL, parallel flow along the field-line, and perpendicular $E_r \times B$ drifts. The parallel flow travels predominately in the toroidal direction, but only the poloidal component is of interest when considering the transport of particles towards or away from the target (see Figure 6 right). The poloidal projection of the parallel velocity is taken as $v_\theta^\parallel = M_\parallel c_s \sin \alpha$ where the field line angle $\alpha \equiv \sin^{-1}(B_\theta/B)$.

Measurements of the plasma potential V_p (Figure 7c,d) indicate that the electric fields are mainly aligned in the radial direction as expected for attached conditions. The $E_r \times B$ drift velocity are calculated as the gradient in V_p and the poloidal projection is taken as $v_\theta^{ExB} = v_{ExB} \cos \alpha$ (see Figure 6 left). v_θ^\parallel , v_θ^{ExB} , and their sum v_θ^{net} , are shown in Figure 7e) for the SN and f) for the LFS SF-.

In the SN, these two terms are of similar magnitude but opposite sign such that these fluxes partially cancel out. The $E_r \times B$ drift is pointing down towards the outer divertor and v_θ^\parallel points upwards away from the outer divertor. Considering either term independently of the other would lead to an erroneous description of the convection in this region. The net poloidal velocity has a magnitude of 0.56 km/s towards the outer divertor, staying constant throughout most of the SOL ($0.1 \text{ cm} < R-R_{sep} < 1.3 \text{ cm}$).

The tendency for the parallel flow to counter-act the $E_r \times B$ drift near the OMP is consistent with analytical descriptions of the Pfirsch-Schlüter flow [29,36–40]. Measurements made in Alcator C-Mod [41] and TCV[36] show good agreement with this analytical description. Closer to the target, the unbalanced flow (i.e. the parallel flow away from the ionization region, towards the target, and driven by parallel pressure gradients) is expected to dominate[40]. The fact that the parallel flow is away from the divertor indicates that the unbalanced flow is not yet dominant at the divertor entrance.

A different behavior is seen for the LFS SF- (Figure 7d) where the $v_\theta^{net} \sim 0$ inside the secondary separatrix indicating a decrease in convection in the region $0.1 \text{ cm} < R-R_{sep} < 0.4 \text{ cm}$ compared to the SN, i.e. a decrease in convection towards SP2. A strong increase in v_θ^{net} occurs just outside the secondary separatrix flowing towards SP4. The secondary separatrix causes a steepening in V_p and a local increase in E_r (see Figure 7d). The parallel flow also changes sign to flow towards SP4. Rather than counter-acting one another, the two convection components act together to drive particle fluxes towards SP4. v_θ^{net} reaches a peak of 1.9km/s at $R-R_{sep} = 0.85 \text{ cm}$, at which point the Bohm-Chodura criterion [42] has been satisfied ($M_\parallel = 0.2$, $v_{ExB}/c_s \tan \alpha = 0.8$) even though these measurements have been taken far from the target (remaining L_\parallel to target = 8m).

In order to quantify the convected heat-fluxes towards each strike-point, the heat fluxes for the parallel convection and the $E_r \times B$ drifts are calculated as follows.

The poloidal projection of the parallel heat-flux is calculated by assuming that $T_i = T_e$ as

$$q_\theta^{M_\parallel} = \frac{B_{\theta \text{ OMP}}}{B_\theta} \sin(\alpha) \cdot n_e c_s M_\parallel \left(5kT_e + \frac{1}{2} m_i v_\parallel^2 \right) \quad (1)$$

and the poloidal projection of the ExB heat-flux is taken as

$$q_{\theta}^{E \times B} = \frac{B_{\theta OMP}}{B_{\theta}} \cos(\alpha) \cdot n_e \frac{E_r}{B} \left(5kT_e + \frac{1}{2} m_i v_{\parallel}^2 \right) \quad (2)$$

where the fluxes have been normalized to the OMP by accounting for poloidal and total flux expansion using the factor $B_{\theta OMP}/B_{\theta}$. This normalization term is needed due to the choice of R-R_{sep} as the flux coordinate and is important when considering the integral in eqn(4) since a flux in the poloidal direction Γ_{θ} is divergence free iff $\Gamma_{\theta}/B_{\theta} = \text{constant}$ [41,43].

$q_{\theta}^{M_{\parallel}}$ (dashed lines) and $q_{\theta}^{E \times B}$ (solid lines) are plotted in Figure 7 (g,h) along with the net heat convection $q_{\theta}^{conv net} = q_{\theta}^{M_{\parallel}} + q_{\theta}^{E \times B}$. The conducted heat-flux is estimated using the classical Spitzer parallel heat conduction equation assuming that the target $T_e = 0$ with a correction for the variation in the major radius of the target[44,45]

$$q_{\theta}^{cond} = \sin(\alpha) \left(\frac{2\kappa_{0e}}{7L_{\parallel}} T_e^{7/2} \right) \left[\frac{f_R - 1}{\ln(f_R)} \right]_{OMP} \quad (3)$$

where the parallel electron heat conductivity coefficient $\kappa_{0e} = 2000$, and $f_R \equiv R_{target}/R_{OMP}$. $f_R \sim 0.56$ for strike-points on the central column and $f_R \sim 1$ for those on the outer wall. Heat conduction in the ion channel is neglected considering that $\kappa_{0e} \sim 60$ and our earlier assumption to take $T_i = T_e$.

The estimate for q_{θ}^{cond} allow for the magnitudes of the convected heat-fluxes to be placed in context. For the SN (g), $q_{\theta}^{conv net}$ matches q_{θ}^{cond} for the majority of the SOL. For the LFS SF- (h) $q_{\theta}^{conv net}$ is small compared to the SN reference for R-R_{sep} < 0.4cm and small compared to q_{θ}^{cond} . This indicates that heat convection towards SP2 is restricted in the LFS SF- when compared to a reference SN.

In the vicinity of the secondary separatrix $q_{\theta}^{conv net}$ reaches a peak value over 2x larger than q_{θ}^{cond} indicating that convection rather than conduction dominates the heat-fluxes arriving at SP4. Convection towards SP4 in the LFS SF- is enhanced when compared to a reference SN.

Next, the power contributions from conduction and convection will be integrated for each strike-point of the LFS SF-. The values can then be compared against the integrated IR camera power values taken from [26] and shown in Table 1. The power for each component is calculated using:

$$P = \pm \int_a^b 2\pi R_{OMP} q_{\theta} d(R-R_{sep}) \quad (4)$$

where a and b are the R-R_{sep} values for the bounding flux surfaces, e.g. a=0 and b=dR_{x2} for SP2. Note that no calculated value is provided for SP1 or SP3 since no measurements of heat convection are available at the entrance of the inner divertor above SP1 or in the private flux region above SP3.

The disagreement between the IR camera measurements and the heat-conduction model can now be considered directly as $P_{cond} < P_{IR}$ for SP2, and P_{cond} is 3x smaller than P_{IR} for SP4. Furthermore, P_{cond} overestimates the power measured at SP1 by over 40%. While the convected heat-fluxes are acting in the correct directions to account for the mismatches between P_{cond} and P_{IR} (i.e. away from SP1, and towards SP2 and SP4) it is generally incorrect to assume that heat and particle fluxes measured at some distance

upstream will arrive at the target since the ExB drifts are capable of turning to cross the flux surfaces in the radial direction taking particles and heat across the PFR [46–48]. Furthermore, it is important to note that the interplay between particle convection in the SOL, convection in the PFR, impurity radiation, and heat conduction are complex have yet to be fully understood [49–53].

However, the situation is considerably simpler for SP4. The measurements at the divertor entrance are relatively close to the target ($L_{||}$ to target $\sim 8\text{m}$), convection is clearly dominating over other effects, and $P_{IR} = 0$ for SP3 which suggests that power is not being drawn away from SP4 by cross-field transport. Therefore, it is reasonable to assume that the heat convected past the divertor entrance towards SP4 arrives at SP4. The dominant heat convection explains why SP4 receives more power than predicted by the conduction models. These measurements confirm that convection is capable of redistributing heat between the strike-points of the snowflake divertor, and that it is possible to modify and exploit the heat-flux redistribution by making changes to the divertor geometry.

The peak in the convected heat-fluxes towards the secondary separatrix is similar to observations made in recent GBS simulations of the LFS SF-[54]. However, the simulations show significant cross-field convection across the secondary X-point and the activation of SP3, while IR camera measurements in this study show undetectable heat-fluxes at SP3. In previous studies, a small amount of power ($<4\%$ of P_{sol}) was observed at the secondary target of a SF-[21]. The differences are likely due to the fact that the simulations consider significantly higher collisionality than those measured in this study. This suggests that convective heat redistribution among the SF strike-points could be significantly stronger in high collisionality detached conditions. A recent SOLPS-ITER simulation [55] also shows that the secondary X-point of the LFS SF- creates strong electric potential gradients resulting in enhanced drift-based convection both in the poloidal and radial directions.

6 Conclusions

Parallel flows and $E_r \times B$ drifts act together in the presence of the secondary X-point of the LFS SF- to drive power and particles towards SP4. At its peak, $q_{\theta}^{conv net}$ exceeds q_{θ}^{cond} estimates by over 2x indicating that heat convection dominates over heat conduction for SP4. The increased convection is related to the sudden change in divertor geometry on either side of the secondary separatrix, which causes a local increase in E_r and a reversal of $M_{||}$. Compared to the convected fluxes from a reference SN, the LFS SF- shows an increase in heat convection towards SP4 and a decrease in heat convection towards SP2 where the two convective components act in opposite directions, canceling one another out. These findings explain why the power measured at SP4 with the IR camera is higher than that predicted by heat conduction and partly explains why the LFS SF- has a broader effective λ_q than the SN and other SF geometries.

These measurements confirm that convection is capable of redistributing heat between the strike-points of the snowflake divertor, and that it is possible to modify and exploit the heat-flux redistribution by making changes to the divertor geometry.

J_{sat} profiles at the divertor entrance show changes in slope depending on the location of the secondary separatrix and on the magnetic field direction showing that ExB drifts interact with the snowflake divertor geometry. Compared to the OMP, parallel pressure losses of up to 50% were observed, enhancing the role of parallel flows. The direction of the pressure and density imbalances are consistent with the $B \times \nabla B$ and $E_r \times B$ drifts.

Profiles of n_e , T_e , J_{sat} and Γ_r^{turb} at the OMP are largely unaffected by divertor geometry when comparing the SN against the SF+, the LFS SF- or the HFS SF- despite the significant changes in divertor geometry, such as a 2X increase in L_{\parallel} or a 1.8X increase in the major radius of the target. Unlike the profiles at the divertor entrance, the OMP profiles are smooth across the entire SOL, even at the secondary separatrix where $L_{\parallel} \rightarrow \infty$.

7 Acknowledgements

This work was supported by the U.S. Department of Energy under Grant No. DE-SC0010529. The technical contributions of L. Chousal and R. Hernandez are gratefully acknowledged. This work was supported in part by the Swiss National Science Foundation. This work has been carried out within the framework of the EUROfusion Consortium and has received funding from the Euratom research and training programme 2014–2020 under Grant Agreement No. 633053. The views and opinions expressed herein do not necessarily reflect those of the European Commission.

8 References

- [1] Eich T, Leonard A W, Pitts R a., Fundamenski W, Goldston R J, Gray T K, Herrmann A, Kirk A, Kallenbach A, Kardaun O, et al Scaling of the tokamak near the scrape-off layer H-mode power width and implications for ITER *Nucl. Fusion* **53** 093031 (2013) <https://doi.org/10.1088/0029-5515/53/9/093031>
- [2] Loarte A, Lipschultz B, Kukushkin A ., Matthews G ., Stangeby P ., Asakura N, Counsell G ., Federici G, Kallenbach A, Krieger K, et al Chapter 4: Power and particle control *Nucl. Fusion* **47** S203–63 (2007) <https://doi.org/10.1088/0029-5515/47/6/S04>
- [3] Zohm H, Angioni C, Fable E, Federici G, Gantenbein G, Hartmann T, Lackner K, Poli E, Porte L, Sauter O, et al On the physics guidelines for a tokamak DEMO *Nucl. Fusion* **53** 073019 (2013) <https://doi.org/10.1088/0029-5515/53/7/073019>
- [4] Ryutov D D Geometrical properties of a “snowflake” divertor *Phys. Plasmas* **14** 064502 (2007) <https://doi.org/10.1063/1.2738399>
- [5] Piras F, Coda S, Furno I, Moret J-M, Pitts R A, Sauter O, Tal B, Turri G, Bencze A, Duval B P, et al Snowflake divertor plasmas on TCV *Plasma Phys. Control. Fusion* **51** 055009 (2009) <https://doi.org/10.1088/0741-3335/51/5/055009>
- [6] Piras F, Coda S, Duval B P, Labit B, Marki J, Medvedev S Y, Moret J M, Pitzschke A and Sauter O “Snowflake” H mode in a tokamak plasma *Phys. Rev. Lett.* **105** 3–6 (2010) <https://doi.org/10.1103/PhysRevLett.105.155003>
- [7] Soukhanovskii V A, Ahn J-W, Bell R E, Gates D A, Gerhardt S, Kaita R, Kolemen E, Kugel H W, LeBlanc B P, Maingi R, et al “Snowflake” divertor configuration in NSTX *J. Nucl. Mater.* **415** S365–8 (2011) <https://doi.org/10.1016/J.JNUCMAT.2010.07.047>
- [8] Soukhanovskii V A, Ahn J-W, Bell R E, Gates D A, Gerhardt S, Kaita R, Kolemen E, LeBlanc B

- P, Maingi R, Makowski M, et al Taming the plasma–material interface with the ‘snowflake’ divertor in NSTX *Nucl. Fusion* **51** 012001 (2011) <https://doi.org/10.1088/0029-5515/51/1/012001>
- [9] Soukhanovskii V A, Bell R E, Diallo A, Gerhardt S, Kaye S, Kolemen E, LeBlanc B P, McLean A G, Menard J E, Paul S F, et al Snowflake divertor configuration studies in National Spherical Torus Experiment *Phys. Plasmas* **19** 082504 (2012) <https://doi.org/10.1063/1.4737117>
- [10] Soukhanovskii V A, Allen S L, Fenstermacher M E, Lasnier C J, Makowski M A, McLean A G, Meier E T, Meyer W H, Rognlien T D, Ryutov D D, et al Snowflake Divertor Experiments in the DIII-D, NSTX, and NSTX-U Tokamaks Aimed at the Development of the Divertor Power Exhaust Solution *IEEE Trans. Plasma Sci.* **44** 3445–55 (2016) <https://doi.org/10.1109/TPS.2016.2625325>
- [11] Porter G D, Petrie T W, Rognlien T D and Rensink M E UEDGE simulation of edge plasmas in DIII-D double null configurations *Phys. Plasmas* **17** 112501 (2010) <https://doi.org/10.1063/1.3499666>
- [12] Ryutov D D, Cohen R H, Rognlien T D and Umansky M V. The magnetic field structure of a snowflake divertor *Phys. Plasmas* **15** 092501 (2008) <https://doi.org/10.1063/1.2967900>
- [13] Umansky M V, Rognlien T D, Ryutov D D and Snyder P B Edge Plasma in Snowflake Divertor *Contrib. to Plasma Phys.* **50** 350–5 (2010) <https://doi.org/10.1002/ctpp.201010057>
- [14] Meier E T, Soukhanovskii V A, Bell R E, Diallo A, Kaita R, LeBlanc B P, McLean A G, Podestà M, Rognlien T D and Scotti F Modeling detachment physics in the NSTX snowflake divertor *J. Nucl. Mater.* **463** 1200–4 (2015) <https://doi.org/10.1016/J.JNUCMAT.2015.01.007>
- [15] Lunt T, Canal G P, Duval B P, Feng Y, Labit B, McCarthy P, Reimerdes H, Vijvers W A J and Wischmeier M Numerical study of potential heat flux mitigation effects in the TCV snowflake divertor *Plasma Phys. Control. Fusion* **58** (2016) <https://doi.org/10.1088/0741-3335/58/4/045027>
- [16] Labit B, Canal G P, Christen N, Duval B P, Lipschultz B, Lunt T, Nespoli F, Reimerdes H, Sheikh U, Theiler C, et al Experimental studies of the snowflake divertor in TCV *Nucl. Mater. Energy* **12** 1015–9 (2017) <https://doi.org/10.1016/J.NME.2017.03.013>
- [17] Reimerdes H, Canal G P, Duval B P, Labit B, Lunt T, Nespoli F, Vijvers W A J, De Temmerman G, Lowry C, Morgan T W, et al Experimental investigation of neon seeding in the snowflake configuration in TCV *J. Nucl. Mater.* **463** 1196–9 (2015) <https://doi.org/10.1016/j.jnucmat.2014.10.076>
- [18] Soukhanovskii V A A review of radiative detachment studies in tokamak advanced magnetic divertor configurations *Plasma Phys. Control. Fusion* **59** 064005 (2017) <https://doi.org/10.1088/1361-6587/aa6959>
- [19] Reimerdes H, Duval B P, Harrison J R, Labit B, Lipschultz B, Lunt T, Theiler C, Tsui C K, Verhaegh K, Vijvers W A J, et al TCV experiments towards the development of a plasma exhaust solution *Nucl. Fusion* **57** 126007 (2017) <https://doi.org/10.1088/1741-4326/aa82c2>
- [20] Kotschenreuther M, Valanju P, Covele B and Mahajan S Magnetic geometry and physics of advanced divertors: The X-divertor and the snowflake *Phys. Plasmas* **20** 102507 (2013) <https://doi.org/10.1063/1.4824735>
- [21] Reimerdes H, Canal G P, Duval B P, Labit B, Lunt T, Vijvers W A J, Coda S, De Temmerman G, Morgan T W, Nespoli F, et al Power distribution in the snowflake divertor in TCV *Plasma Phys. Control. Fusion* **55** 124027 (2013) <https://doi.org/10.1088/0741-3335/55/12/124027>
- [22] Soukhanovskii V A, Allen S L, Fenstermacher M E, Lasnier C J, Makowski M A, McLean A G, Meyer W H, Ryutov D D, Kolemen E, Groebner R J, et al Developing physics basis for the snowflake divertor in the DIII-D tokamak *Nucl. Fusion* **58** 036018 (2018) <https://doi.org/10.1088/1741-4326/aaa6de>

- [23] Lunt T, Zohm H, Herrmann A, Kallenbach A, Dunne M, Feng Y, Neu R and Wischmeier M Proposal of an alternative upper divertor in ASDEX Upgrade supported by EMC3-EIRENE simulations *Nucl. Mater. Energy* **12** 1037–42 (2017) <https://doi.org/10.1016/J.NME.2016.12.035>
- [24] Lunt T, Canal G P, Feng Y, Reimerdes H, Duval B P, Labit B, Vijvers W A J J, Coster D, Lackner K and Wischmeier M First EMC3-Eirene simulations of the TCV snowflake divertor *Plasma Phys. Control. Fusion* **56** 035009 (2014) <https://doi.org/10.1088/0741-3335/56/3/035009>
- [25] Maurizio R, Duval B P, Labit B, Reimerdes H, Theiler C, Tsui C K, Boedo J, De Oliveira H, Février O, Sheikh U, et al Conduction-based model of the Scrape-Off Layer power sharing between inner and outer divertor in diverted low-density tokamak plasmas *Nucl. Mater. Energy* **19** 372–7 (2019) <https://doi.org/10.1016/J.NME.2019.03.020>
- [26] Maurizio R, Tsui C K, Duval B P, Reimerdes H, Theiler C, Boedo J A, Labit B, Sheikh U, Spolaore M, Team T T Euro M, et al The effect of the secondary x-point on the Scrape-Off Layer transport in the TCV Snowflake Minus divertor *Nucl. Fusion* **59** 016014 (2019) <https://doi.org/10.1088/1741-4326/aae1b>
- [27] Coda S, Agostini M, Albanese R, Alberti S, Alessi E, Allan S, Allcock J, Ambrosino R, Anand H, Andrebe Y, et al Physics research on the TCV tokamak facility: From conventional to alternative scenarios and beyond *Nucl. Fusion* **59** (2019) <https://doi.org/10.1088/1741-4326/ab25cb>
- [28] Boedo J A, Crocker N, Chousal L, Hernandez R, Chalfant J, Kugel H, Roney P and Wertenbaker J Fast scanning probe for the NSTX spherical tokamak *Rev. Sci. Instrum.* **80** 123506 (2009) <https://doi.org/10.1063/1.3266065>
- [29] Stangeby P C *The Plasma Boundary of Magnetic Fusion Devices* (New York: Taylor & Francis Group) (2000) <https://doi.org/10.1088/0741-3335/43/2/702>
- [30] Tsui C K, Boedo J A, Stangeby P C and the TCV Team Accounting for Debye sheath expansion for proud Langmuir probes in magnetic confinement fusion plasmas *Rev. Sci. Instrum.* **89** 013505 (2018) <https://doi.org/10.1063/1.4995353>
- [31] Hutchinson I H *Principles of Plasma Diagnostics: Second Edition* vol 44 (Cambridge University Press) (2002) <https://doi.org/10.1088/0741-3335/44/12/701>
- [32] Boedo J A, Myra J R, Zweben S, Maingi R, Maqueda R J, Soukhanovskii V A, Ahn J W, Canik J, Crocker N, D'Ippolito D A, et al Edge transport studies in the edge and scrape-off layer of the National Spherical Torus Experiment with Langmuir probes *Phys. Plasmas* **21** (2014) <https://doi.org/10.1063/1.4873390>
- [33] Boedo J A, Rudakov D L, Moyer R A, McKee G R, Colchin R J, Schaffer M J, Stangeby P G, West W P, Allen S L, Evans T E, et al Transport by intermittency in the boundary of the DIII-D tokamak *Phys. Plasmas* **10** 1670–7 (2003) <https://doi.org/10.1063/1.1563259>
- [34] Boedo J A, Rudakov D, Moyer R, Krasheninnikov S, Whyte D, McKee G, Tynan G, Schaffer M, Stangeby P, West P, et al Transport by intermittent convection in the boundary of the DIII-D tokamak *Phys. Plasmas* **8** 4826–33 (2001) <https://doi.org/10.1063/1.1406940>
- [35] Maurizio R, Elmore S, Fedorczak N, Gallo A, Reimerdes H, Labit B, Theiler C, Tsui C K, Vijvers W A J, Team T T, et al Divertor power load studies for attached L-mode single-null plasmas in TCV *Nucl. Fusion* **58** 016052 (2018) <https://doi.org/10.1088/1741-4326/aa986b>
- [36] Pitts R A, Horacek J, Fundamenski W, Garcia O E, Nielsen A H, Wischmeier M, Naulin V and Juul Rasmussen J Parallel SOL flow on TCV *J. Nucl. Mater.* **363–365** 505–10 (2007) <https://doi.org/10.1016/j.jnucmat.2006.12.065>
- [37] Boedo J A Edge turbulence and SOL transport in tokamaks *J. Nucl. Mater.* **390–391** 29–37 (2009) <https://doi.org/10.1016/j.jnucmat.2009.01.040>

- [38] Smick N, LaBombard B and Pitcher C S Plasma profiles and flows in the high-field side scrape-off layer in Alcator C-Mod *J. Nucl. Mater.* **337–339** 281–5 (2005) <https://doi.org/10.1016/J.JNUCMAT.2004.09.035>
- [39] LaBombard B, Rice J ., Hubbard A ., Hughes J ., Greenwald M, Irby J, Lin Y, Lipschultz B, Marmor E ., Pitcher C ., et al Transport-driven Scrape-Off-Layer flows and the boundary conditions imposed at the magnetic separatrix in a tokamak plasma *Nucl. Fusion* **44** 1047–66 (2004) <https://doi.org/10.1088/0029-5515/44/10/001>
- [40] Rozhansky V, Molchanov P, Voskoboynikov S, Counsell G, Kirk A, Coster D and Schneider R Modeling of the parametric dependence of the edge toroidal rotation for MAST and ASDEX Upgrade *J. Nucl. Mater.* **363–365** 664–8 (2007) <https://doi.org/10.1016/j.jnucmat.2007.01.265>
- [41] Smick N, LaBombard B and Hutchinson I H Transport and drift-driven plasma flow components in the Alcator C-Mod boundary plasma *Nucl. Fusion* **53** 023001 (2013) <https://doi.org/10.1088/0029-5515/53/2/023001>
- [42] Stangeby P C The Bohm-Chodura plasma sheath criterion *Phys. Plasmas* **2** 702–6 (1995) <https://doi.org/10.1063/1.871483>
- [43] Helander P and Sigmar D J *Collisional transport in magnetized plasmas* (Cambridge University Press) (2002) <https://doi.org/10.1017/cbo9780511770609.006>
- [44] Stangeby P *Modified 2 Point Model of the SOL to allow for variation in R* (2011)
- [45] Kotschenreuther M, Valanju P, Mahajan S, Zheng L, Pearlstein L, Bulmer R, Canik J and Maingi R The super X divertor (SXD) and a compact fusion neutron source (CFNS) *Nucl. Fusion* **50** 035003 (2010) <https://doi.org/10.1088/0029-5515/50/3/035003>
- [46] Boedo J A, Schaffer M J, Maingi R and Lasnier C J Electric field-induced plasma convection in tokamak divertors *Phys. Plasmas* **7** 1075 (2000) <https://doi.org/10.1063/1.873915>
- [47] Schaffer M J, Boedo J A, Moyer R A, Carlstrom T N and Watkins J G Large $E \times B$ convection near the divertor X -point *J. Nucl. Mater.* **293** 530–6 (2001)
- [48] Schaffer M J, Bray B D, Boedo J A, Carlstrom T N, Colchin R J, Hsieh C L, Moyer R A, Porter G D, Rognlien T D and Watkins J G EXB circulation at the tokamak divertor X point *Phys. Plasmas* **8** 2118–24 (2001) <https://doi.org/10.1063/1.1352597>
- [49] Chankin A V, Corrigan G, Groth M, Stangeby P C and contributors J Influence of the $E \times B$ drift in high recycling divertors on target asymmetries *Plasma Phys. Control. Fusion* **57** 095002 (2015) <https://doi.org/10.1088/0741-3335/57/9/095002>
- [50] Chankin A ., Coster D ., Asakura N, Bonnin X, Conway G ., Corrigan G, Erents S ., Fundamenski W, Horacek J, Kallenbach A, et al Discrepancy between modelled and measured radial electric fields in the scrape-off layer of divertor tokamaks: a challenge for 2D fluid codes? *Nucl. Fusion* **47** 479–89 (2007) <https://doi.org/10.1088/0029-5515/47/5/013>
- [51] Chankin A ., Coster D ., Asakura N, Corrigan G, Erents S ., Fundamenski W, Müller H ., Pitts R ., Stangeby P . and Wischmeier M A possible role of radial electric field in driving parallel ion flow in scrape-off layer of divertor tokamaks *Nucl. Fusion* **47** 762–72 (2007) <https://doi.org/10.1088/0029-5515/47/8/006>
- [52] Stangeby P . and Chankin A . Simple models for the radial and poloidal $E \times B$ drifts in the scrape-off layer of a divertor tokamak: Effects on in/out asymmetries *Nucl. Fusion* **36** 839–52 (1996) <https://doi.org/10.1088/0029-5515/36/7/I02>
- [53] Ghendrih P, Auphan T, Bensiali B, Bilanceri M, Bodi K, Bonnement A, Bufferand H, Chiavassa G, Ciraolo G, Futtersack R, et al Divertor imbalance and divertor density regimes for ballooned cross-field turbulence *J. Nucl. Mater.* **438** S368–71 (2013)

<https://doi.org/10.1016/J.JNUCMAT.2013.01.070>

- [54] Giacomini M, Stenger L N and Ricci P Turbulence and flows in the plasma boundary of snowflake magnetic configurations *Nucl. Fusion* **60** 024001 (2020) <https://doi.org/10.1088/1741-4326/ab6435>
- [55] Pan O, Lunt T, Wischmeier M, Coster D and Stroth U SOLPS-ITER modeling with activated drifts for a snowflake divertor in ASDEX Upgrade *Plasma Phys. Control. Fusion* **62** 045005 (2020) <https://doi.org/10.1088/1361-6587/ab7108>